Arc Behavior and Melting Rate in the VP-GMAW Process

Droplet melting analysis performed using high-speed video synchronized with high-speed data acquisition was used to evaluate arc behavior and melting rate

D. D. HARWIG, J. E. DIERKSHEIDE, D. YAPP, and S. BLACKMAN

ABSTRACT. This paper evaluates the arc behavior and melting rate in the variable polarity (VP) gas metal arc welding (GMAW) process. Droplet melting analysis was performed using high-speed video that was synchronized with high-speed data acquisition. Melting rate measurements were found to be very dependent on current waveform, polarity, droplet size, and metal transfer, if it occurred, for each waveform period. The transient conditions of current waveform and metal transfer produced rapid changes in arc behavior that influenced the melting at the electrode tip and growing droplet. The concentrated melting theory was developed to explain the significant increase in electrode extension burnoff and droplet growth rate that occurred at short electrode negative (EN) time as a function of current, and during electrode positive (EP) peak pulse when the prepulse droplet volume was small. The highest electrode extension burnoff and droplet growth rate occurred when the arc was permitted to climb over the solid electrode tip producing rapid concentrated melting. Likewise, large molten droplets were found to promote a negative electrode extension burnoff and a decreased droplet growth rate. The arc rooted on large droplets providing additional heating but limited electrode melting. The droplet burnoff rate (DBR) method was developed and found to yield good experimental measurements for the arc melting and resistive heating coefficients used in a second-order melting rate equation developed for a complex waveform process, like VP-GMAW. For the EN period, the EN time affected the melting rate as a function of EN current. The greater melting rate that occurred at low EN time was measured by the changes in the resistive heating coefficient. Concentrated arc melting of the electrode extension at low EN time caused the slope of the burnoff diagram to increase, which represented the resistive heating coefficient. The melting rate of the EP pulse was related to the prepulse droplet volume. Large prepulse droplets decreased the arc melting coefficient, which could be negative, which meant the electrode extension was increasing and the arc length was decreasing in that waveform period.

D. D. HARWIG is with Thermadyne Industries, West Lebanon, N.H. J. E. DIERKSHEIDE is with Northrop Grumman Newport News, Newport News, Va. D. YAPP and S. BLACKMAN are with Cranfield University, Bedfordshire, UK.

Introduction

Gas metal arc welding (GMAW) technology has advanced considerably over the past two decades due to the development of microprocessor-controlled, solid-state power supplies. Currently, power supplies are designed for constant voltage (CV) GMAW, pulse GMAW (GMAW-P), and pulse short circuit GMAW (Refs. 1–4), and more recently variable polarity (VP) GMAW (Refs. 5–11). However, there was a lack of understanding of VP-GMAW principles. The limited research was mostly from Japan, where the process was introduced in 1988 (Refs. 5–7). Since the early 1990s, several hundred power supplies have been sold in the United States. Unfortunately, many industrial users do not understand the benefits of this technology since limited research has been published in the United States (Refs. 3, 4, 10, 11). This has deterred wide-scale implementation of VP-GMAW throughout industry. The power supplies offered by the Japanese manufacturers have preprogrammed algorithms and are presently limited to welding of mild steel, stainless steel, and aluminum at currents up to 350 A where the benefit has been the welding of thin-gauge structures with large root openings (Refs. 10–12).

KEYWORDS

Metal Transfer
Droplet
Drops
Arc Behavior
Melting Rate
GMAW
Variable Polarity

The metal transfer process for VP-GMAW begins with droplet formation in the EN period where large droplets form on the end of the electrode — Fig. 1. The waveform switches to the electrode positive background (EPB) period to maintain the arc at low current. The electrode positive peak (EPP) period is used to transfer the droplets by using a high-current pulse that squeezes the droplet off the electrode tip forming a drop. The drops transfer across the arc into the weld pool. The VP-GMAW waveform can be designed to provide a range of heat inputs for a given wire feed speed, thus allowing optimization of the travel speed for different weld deposit size applications.

There are many factors that affect the droplet formation and transfer process that are not understood. The behavior of VP-GMAW arcs and metal transfer had not been published in the literature (Ref. 12). Based on this, there appeared to be a technology gap on the principles controlling melting rate, metal transfer, and arc behavior of the VP-GMAW process. The general melting rate equation for DC GMAW was developed by Lesnewich (Ref. 13). Based on his research, a well-accepted form of the melting rate equation has been established for a given electrode type and diameter for spray metal transfer modes as follows:

$$MR_{dc} = \alpha I + \beta L I^2 \qquad (1)$$

where MR_{dc} = (mm/s), α = arc melting coefficient (mm/s-amp), I = current (amps), β = resistive heating coefficient (amps^2-s)$^{-1}$, and L = electrode extension (mm).

The first term of this equation (αI) represents the contribution from arc melting, and the second term of the equation ($\beta L I^2$) represents the contribution from electrode extension resistance heating. The arc melting term is dependent on the polarity, and electrode type and size. For EN heating, the arc melting term is also a

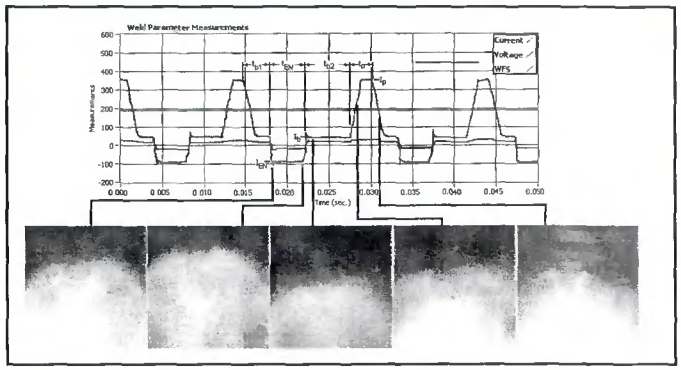

Fig. 1 — VP-GMAW waveform and droplet growth transfer process.

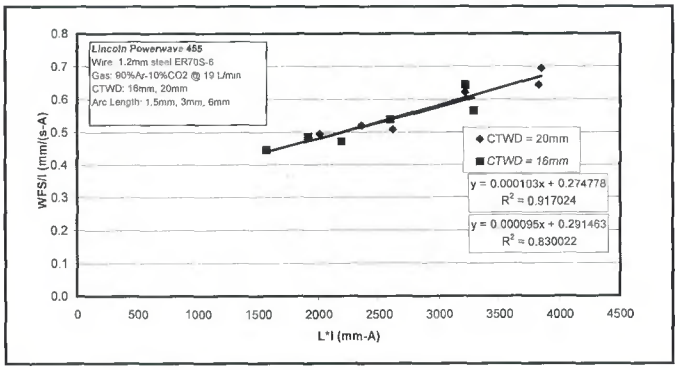

Fig. 2 — Burnoff diagram for spray metal transfer using a EP CV power supply for 1.2-mm steel electrode at various arc lengths and 16- and 19-mm CTWD. Note: equations are ordered in the same vertical order as the legend symbols.

function of shielding gas and electrode activation. The resistive heating term is based on I^2R heating that occurs in the electrode extension.

Allum (Ref. 14) and Richardson (Ref. 15) both attempted to use this fundamental melting rate equation to explain the behavior of GMAW-P. Their research assumed the current waveform was totally responsible for changes in melting rate. Under this assumption, α and β coefficients were believed to be constant for each electrode polarity, type, and size. The improved melting rate was solely attributed to increases in I^2R heating in the electrode extension due to the high current pulse. The research performed here showed the transient behavior of the arc at the electrode tip has a significant effect on melting rate for identical peak pulse waveforms. The resistive heating (I^2R) effect was secondary in importance compared to the arc melting effect using pulsed waveforms.

Richardson showed that the burnoff diagram (BD) technique can be used to determine empirically the α and β coefficients for GMAW processes, especially CV processes that have uniform metal transfer. The burnoff diagram (Fig. 2) plots the burnoff rate (MR/I) against the electrode extension heating factor, $F_L = (L * I)$ providing a line for a given electrode polarity, type, and size over a range of wire feed speeds (WFS), electrode extensions, and arc lengths. When the BD was applied to GMAW-P waveforms, both Allum and Richardson used an effective current parameter to make the data fit the burnoff diagram. This approach made quantitative prediction of melting rate using different waveforms very difficult and accuracy was marginal. In this investigation, it was decided to use the BD to study electrode melting rate based on the droplet growth and electrode extension position in each period of VP-GMAW waveforms. This approach gave a good data fit and allowed characterization of arc and melting rate behavior in complex waveforms.

To establish working pulse parameters, researchers (Refs. 14, 16–18) established a detachment parameter that described the GMAW-P pulse energy requirements for metal transfer. The detachment parameter was believed to satisfy the relationship for improved resistive heating for pulse waveforms. The detachment parameter was based on the energy required to achieve one drop per pulse conditions. However, industry has been plagued with cases that show that a simple relationship like this and others (Ref. 19) cannot be used to predict melting rate and metal transfer stability. In fact, most modern power supplies have empirically developed pulse parameters that are not based on a well-defined algorithm (Ref. 20). To remedy the technology gap, most power supply manufacturers provide waveform parameter development tools that allow the user to optimize metal transfer stability for a given melting rate. The user lacking fundamental knowledge usually develops pulse parameters through trial and error. This investigation showed that the EN period and/or EP background period controlled the EP prepulse droplet volume. The melting rate of identical EP pulses was dependent on the prepulse droplet size. Based on these observations, the detachment parameter can only be used under a small range of pulse waveforms that have a similar prepulse droplet size. Wide changes in pulse parameters that affect droplet size will surely lead to errors using the detachment parameter approach.

For VP-GMAW, the research reviewed (Refs. 4–11, 21–33) has focused on the development of power supplies that permit waveform control, working VP pulse parameters, and commercialization of equipment. The arc behavior and its interactive effects on melting rate were not understood for VP-GMAW waveforms. Engineering relationships were needed to provide an analytical approach for designing waveforms and predicting the resulting melting rate. This technology will promote deployment of VP-GMAW in applications, like welding sheet steel and cladding vessels that can benefit from the lower heat input and higher melting rates of this process.

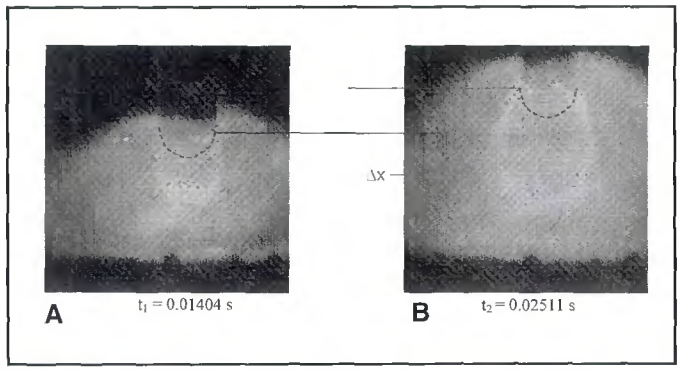

Fig. 3 — Electrode extension burnoff during droplet growth in EN period.

Experimental Procedure

The objectives of this investigation were as follows:

1) Develop an electrode melting rate measurement method that can accurately solve for the α and β coefficients of advanced waveform processes, like VP-GMAW and GMAW-P.

2) Determine the effects of VP-GMAW waveform on electrode melting, and the droplet growth and detachment process.

3) Measure the change in α and β coefficients for a full range of VP-GMAW waveforms and determine the underlying mechanisms for differences due to polar-

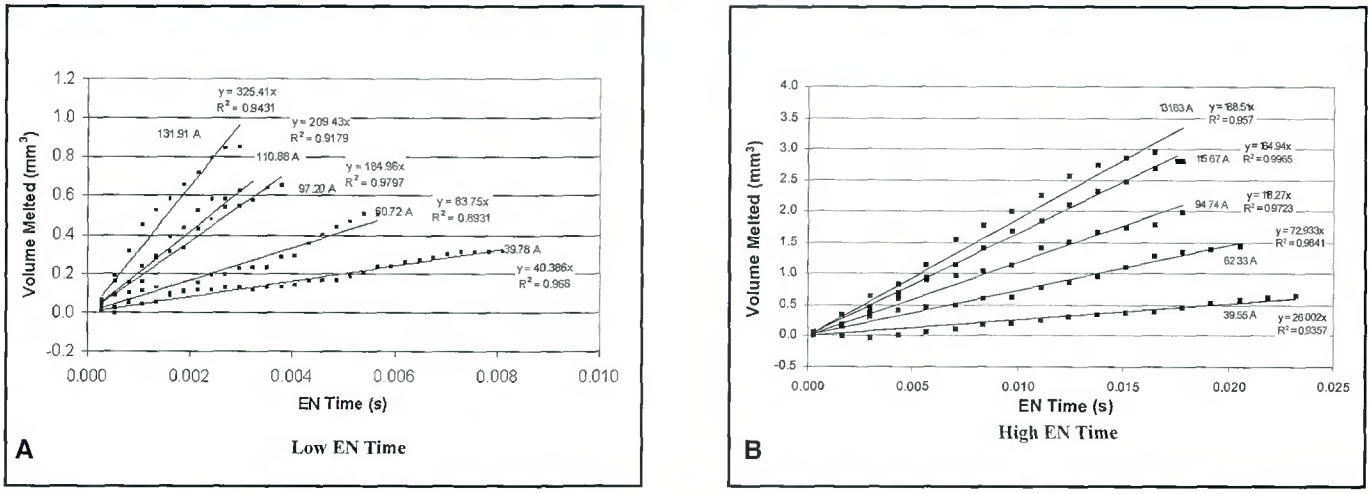

Fig. 4 — Droplet growth during the EN period at minimum and maximum time measured using high-speed video tests. A — Low EN time; B — high EN time.

Table 1 — DBR Measurements for EN Waveform Parameters

Weld No.	WFS_{DAQ} (mm/s)	Δx (mm)	t_{EN} (s)	$\Delta x/t_{EN}$ (mm/s)	MR_{EN} (mm/s)	V_d (mm^3)	V_D (mm^3/s)	I_{EN} (A)	BR (mm/(s A))	F_L (mm A)	f (Hz)	%EN (%)
0–42	39.32	–0.074	0.0083	–8.896	30.42	0.258	31.22	40.03	0.761	513.92	41.75	34.57
30–42	39.01	–0.005	0.0113	–0.451	38.56	0.446	39.57	39.81	0.968	512.48	44.04	49.63
60–42	38.26	0.020	0.0143	1.423	39.68	0.581	40.71	39.68	1.001	511.26	45.31	64.70
90–42	38.52	–0.097	0.0173	–5.582	32.93	0.584	33.79	39.56	0.833	507.45	39.51	68.31
120–42	38.96	–0.010	0.0202	–0.503	38.45	0.797	39.45	39.55	0.972	509.01	39.01	78.76
150–42	38.95	–0.041	0.0232	–1.752	37.20	0.885	38.17	39.55	0.941	508.40	34.72	80.52
0–63	59.28	0.076	0.0056	13.553	72.83	0.420	74.73	60.72	1.201	784.08	66.94	37.64
30–63	59.28	0.127	0.0086	14.767	74.04	0.653	75.97	62.30	1.189	806.07	66.07	56.82
60–63	59.28	0.157	0.0116	13.623	72.90	0.865	74.80	62.33	1.169	807.41	57.80	66.82
90–63	59.28	0.155	0.0145	10.663	69.94	1.043	71.76	62.39	1.121	808.10	50.03	72.69
120–63	59.28	0.366	0.0175	20.877	80.15	1.441	82.24	62.49	1.283	815.99	42.98	75.30
150–63	59.28	0.152	0.0205	7.423	66.70	1.405	68.44	62.33	1.070	807.25	36.90	75.76
0–85	80.34	0.276	0.0040	68.415	148.76	0.616	152.64	97.20	1.528	1264.92	74.03	29.89
30–85	83.01	0.502	0.0070	71.409	154.42	1.113	158.46	96.24	1.603	1263.26	71.78	50.43
60–85	81.65	0.592	0.0100	58.946	140.60	1.448	144.27	95.36	1.474	1255.96	61.51	61.76
90–85	81.83	0.528	0.0130	40.703	122.54	1.632	125.73	95.07	1.289	1249.17	51.00	66.20
120–85	81.96	0.478	0.0159	30.014	111.98	1.828	114.90	95.05	1.178	1246.48	43.99	69.99
150–85	81.25	0.546	0.0189	28.833	110.08	2.139	112.95	94.91	1.160	1247.83	38.90	73.68
0–106	102.24	0.218	0.0032	68.476	170.72	0.559	175.17	110.61	1.546	1436.18	91.04	29.04
30–106	102.24	0.650	0.0062	105.217	207.46	1.316	212.87	112.90	1.837	1490.29	74.98	46.34
60–106	102.24	0.737	0.0092	80.503	182.74	1.716	187.51	115.19	1.587	1525.50	60.99	55.81
90–106	102.24	0.785	0.0121	64.864	167.10	2.075	171.46	115.64	1.445	1534.25	51.00	61.71
120–106	102.24	0.897	0.0151	59.300	161.54	2.506	165.75	115.60	1.397	1540.17	42.19	63.79
150–106	102.24	0.970	0.0181	53.666	155.91	2.892	159.97	115.67	1.348	1545.37	37.12	67.11
0–127	123.28	0.426	0.0031	136.979	260.26	0.831	267.05	133.60	1.948	1748.63	91.09	28.34
30–127	123.49	0.754	0.0061	123.265	246.76	1.550	253.20	133.30	1.851	1766.52	71.83	43.96
60–127	123.55	0.813	0.0091	89.319	212.87	1.988	218.43	132.00	1.613	1753.14	58.06	52.83
90–127	123.31	0.914	0.0121	75.695	199.01	2.467	204.20	131.37	1.515	1751.45	49.68	60.01
120–127	123.21	0.554	0.0150	36.964	160.17	2.462	164.35	131.88	1.214	1734.47	43.60	65.31
150–127	123.94	0.777	0.0181	42.989	166.93	3.097	171.29	131.63	1.268	1745.89	38.06	68.81

Note: Weld No. = %EN pendant setting, wire feed speed setting.

ity and waveform.

4) Compare the measured α and β coefficients to measurements made by prior researchers to determine the validity of the DBR method that employed the BD to solve for the coefficients.

Constant arc length, contact tip-to-work distance (CTWD), and deposit area tests were used to study the effects of VP-GMAW waveform (Fig. 1) on melting rate. The power supply was an OTC AC/MIG 200. The machine was set up to use the preprogrammed waveform algorithms for 1.2-mm mild steel electrodes. The filler metal was 1.14-mm- (0.045-in.-) diameter ER70S-6 uncoated steel wire used with 90Ar-10CO_2 shielding gas at 18.8 L/min. The steel electrode was manufactured by National Standard per AWS A5.18 by the trade name of NS-115. The diameter of the electrode was measured with a micrometer prior to welding since the diameter was used to calibrate the high-speed video (HSV) dimensional analysis software in each test. High-speed video synchronized with high-speed data acquisition (DAQ) was used to capture

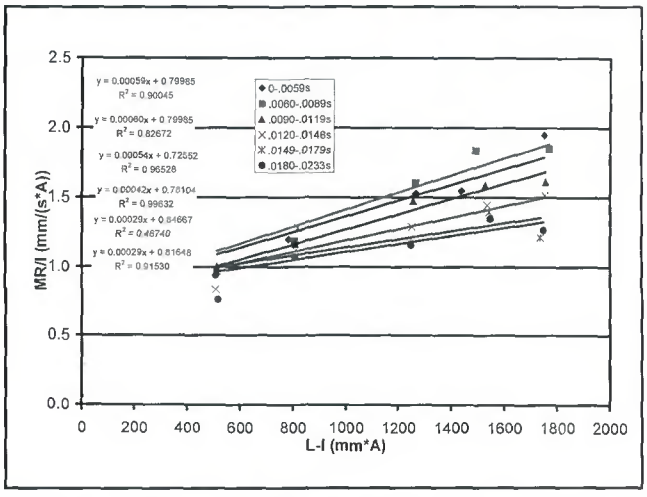

Fig. 5 — Burnoff diagram for EN waveforms for 1.2-mm steel electrode at 3-mm arc length and 16-mm CTWD. Note: equations are ordered in the same vertical order as the legend symbols.

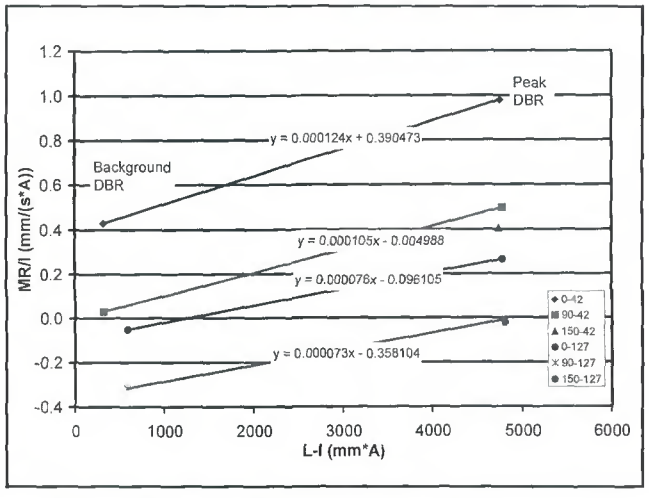

Fig. 6 — Burnoff diagram for EP waveforms for 1.2-mm steel electrode at 3-mm arc length and 16-mm CTWD.

the wire feed speed, current, voltage, and metal transfer of each waveform test.

The test matrix was designed to characterize a range of waveforms that varied the percent EN at five wire feed speeds ranging from 40 to 123 mm/s (Table 1). The EN current was increased from 40 to 133 A as the wire feed speed was increased from 40 to 123 mm/s, respectively. The actual DAQ wire feed speed varied slightly from the machine test setting. The EN current strategy was almost linear over this wire feed range since it was approximately 1 to 1.1 A EN to each mm/s of wire feed speed, respectively. The power transferred to the work was controlled by setting the percent EN, which changed the pulse frequency, *f,* and the EN time. On the AC/MIG 200 power supply, the percent EN pendant setting ranged from –150 to 150. The waveforms generated using the percent EN setting from 0 to –150 were GMAW-P type waveforms, therefore, these settings were not studied in detail. Percent EN increased as the pendant setting increased from 0 to 150 at each WFS. The arc length trim feature varied pulse frequency by varying EPB time, to control arc length.

Droplet Burnoff Rate Method

The droplet burnoff rate (DBR) method was based on measuring the droplet melting rate (mm/s) during each period, corresponding waveform (current and time), and electrode/droplet dimensions that affect these measurements. These data were then used to create burnoff diagrams (BDs) to solve for the melting rate coefficients. The BD plots electrode burnoff rate, BR (mm/s-A) vs. the electrode extension heating factor, F_L (mm-A). The Fig. 2 BD was for CV spray metal transfer with an ER70S-6 electrode. Here, a matrix of spray welding conditions was found to yield a linear relationship demonstrating the validity of the BD method. The intercept and slope of the line made with this diagram equaled the α and β coefficients. This approach was applied to each waveform period.

A Phantom V5.0 high-speed video camera, which used a complementary metal oxide semiconductor (CMOS) array, was set up to allow viewing of the growing droplet at the electrode tip and subsequent drop detachment. Shutter speed was adjusted to allow viewing of the metal transfer without using laser backlighting. The shutter speed was optimized for the waveform period being studied and for measuring arc length. The shutter settings for DBR measurements were 70 microsecond exposure and 10 microsecond extreme dynamic range. The latter feature switched the shutter speed to the higher speed to compensate for the very bright arc flash during pulse welding. The arc length was trimmed using the control pendant to 3 mm nominal at drop detachment between the electrode tip and weld pool surface. The high-speed video sampling frequency was nominally set at 3700 Hz. This frequency optimized the image size for measuring the droplet growth and electrode extension providing 512 x 512 pixel resolution. The HSV images were used to measure change in electrode extension (Δx) during each waveform period. Graphical software tools were used

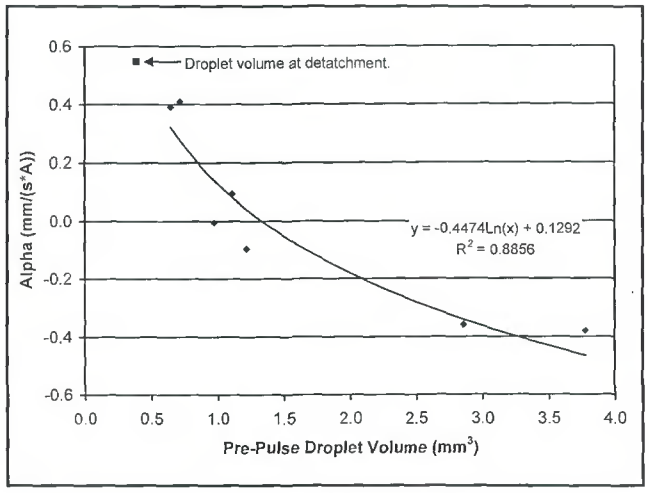

Fig. 7 — EP prepulse droplet volume effects on arc melting coefficient.

to calibrate distance measurements by marking and entering the wire diameter dimension in the first frame prior to measuring electrode extension changes. The electrode solid-liquid droplet interface position was measured in the first and last frame of this period to calculate Δx as shown in Fig. 3. During droplet formation, the electrode extension length either burned off or increased in length, with the current waveform to balance the melting rate. For this project, the electrode melting rate (MR) for each period of the waveform was determined empirically by adding the electrode extension burnoff rate to the WFS_{DAQ}. The MR for each waveform period (EN, EPB, EPP) was

$$MR_{(EN,EPP,EPB)} = \frac{\Delta x}{t_2 - t_1} + WFS_{DAQ} \quad (2)$$

where Δx is the electrode extension

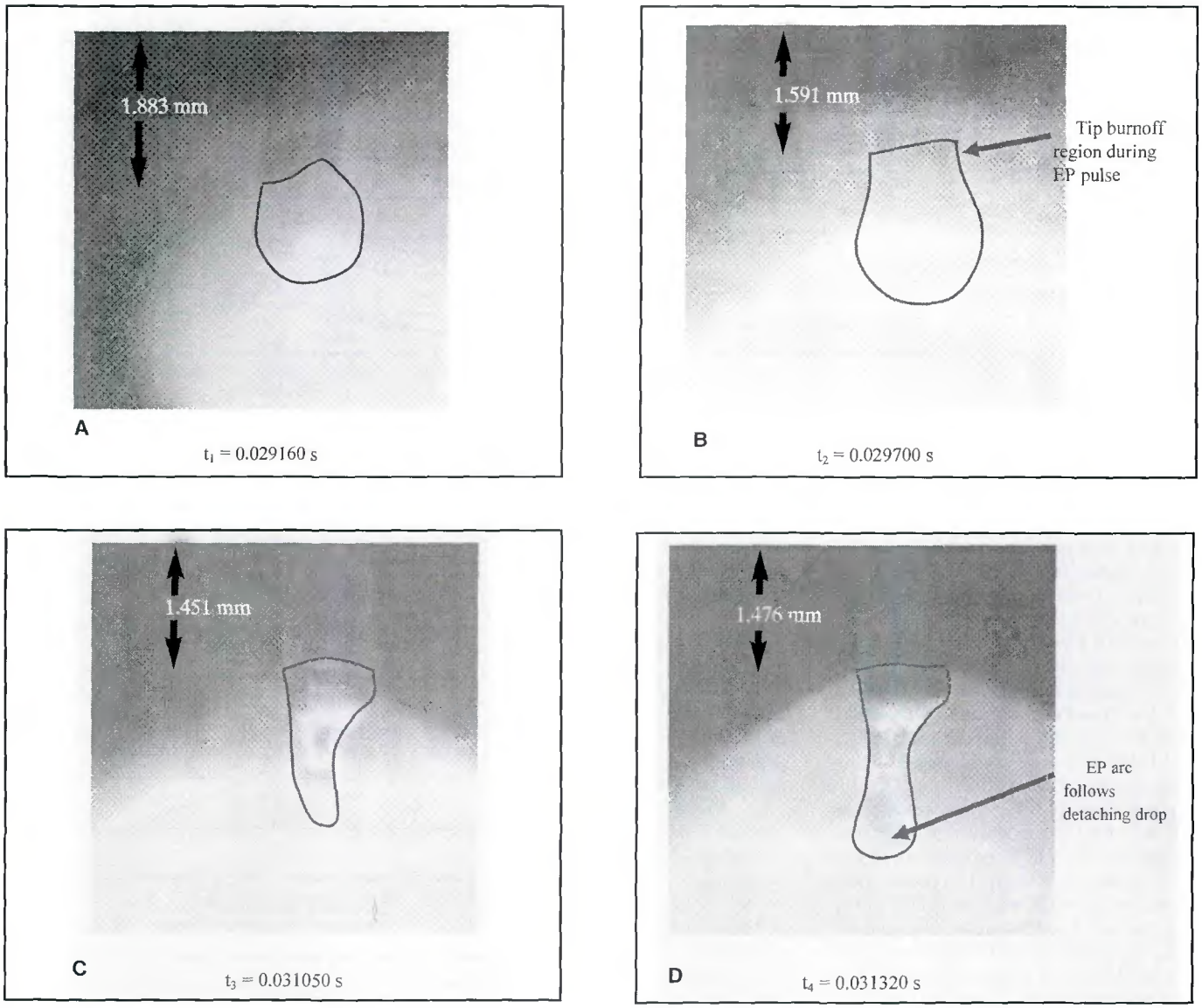

Fig. 8 — High-speed video image showing small prepulse droplet volume effect on EPP arc. A — t_1 = 0.029160 s; B — t_2 = 0.029700 s; C — t_3 = 0.031050 s; D — t_4 = 0.031320 s.

burnoff, which equals the length of change in solid-liquid interface position from initial time (t_1) to final time (t_2) and WFS_{DAQ} is wire feed speed measured with the data acquisition during that period. The Δx was measured by calibrating the high-speed video frames to the wire diameter (1.14 mm) and recording the droplet-electrode interface position at initial and final times for each period. The sign convention used for Δx required that positive interface growth be upward (toward the solid wire). Figure 3A shows the interface position at the beginning of the EN cycle. Figure 3B shows the interface position at the end of the EN cycle. In this case, the time elapsed throughout the cycle is 0.01107 s and growth is in the positive direction ($\Delta x > 0$). The droplet volume growth rate is proportional to the melting rate defined by Equation 2 and the wire area, A_w, which was 1.02 mm^2 (0.00159 in.^{2}), assuming the solid-liquid droplet interface shape does not change. Therefore, the droplet volume growth rate (V_D) in each period was

$$V_D = \left(\frac{\Delta x}{t_2 - t_1} + WFS_{DAQ} \right) \cdot A_w \qquad (3)$$

The electrode extension heating factor (F_L) for each waveform period was determined as follows:

$$F_{L(EN,EPB,EPP)} = L \cdot I_{EN,EPB,EPP} \qquad (4)$$

The average electrode extension was based on the change in electrode extension length, Δx, relative to the initial electrode extension, Lo, during the period of evaluation:

$$L_{EN,EPB,EPP} = Lo + \frac{\Delta x}{2} \qquad (5)$$

The average melting rate can be determined by summing the MR for each period and multiplying the waveform frequency, f, with the following equation:

$$MR_{AVG} = \left(\begin{array}{l} \left(MR_{(EN)} \cdot t_{EN} \right) + \left(MR_{(EPB)} \cdot t_{EPB} \right) \\ + \left(MR_{(EPP)} \cdot t_{EPP} \right) \end{array} \right) \cdot f \qquad (6)$$

The MR_{AVG} should equal the wire feed speed for a stable VP-GMAW waveform. The percent EN of each waveform based on time was determined from the waveform DAQ. The percent EN was deter-

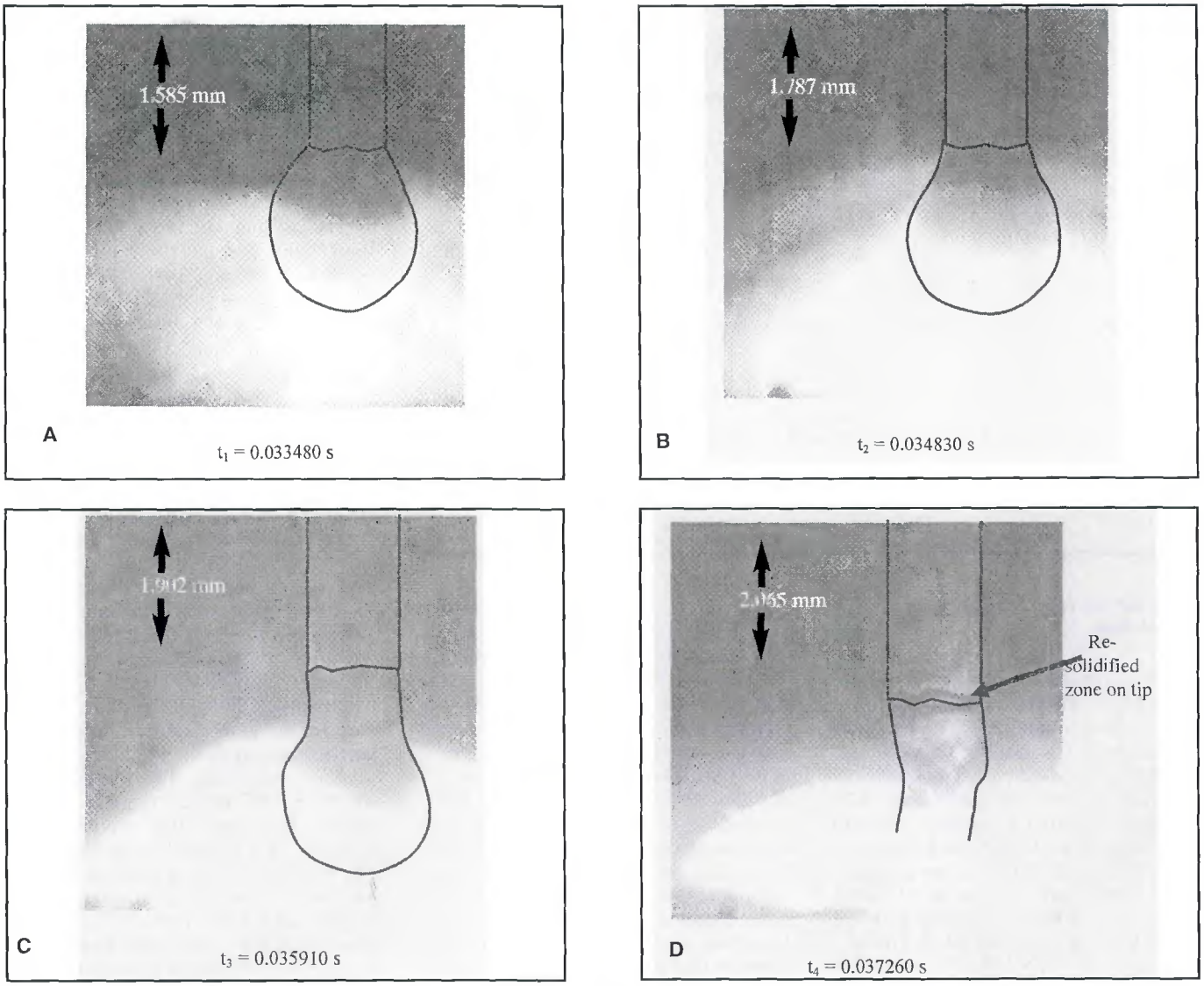

Fig. 9 — High-speed video image showing large prepulse droplet volume effect on EPP arc. A — t_1 = 0.033480 s; B — t_2 = 0.034830 s; C — t_3 = 0.035910 s; D — t_4 = 0.037260 s.

mined using the following equation:

$$\%EN = (f \cdot t_{EN}) \cdot 100\% \qquad (7)$$

where f is the pulse frequency and t_{EN} is time spent in EN polarity. Percent EN was related to waveform parameters to determine relationships for process stability, such as the effects of I_{EN} and t_{EN} on melting rate. The EN ratio was calculated on some tests to compare the arc melting potency with different waveforms as follows:

$$ENratio = \frac{I_{EN}t_{EN}}{\left(I_p t_p\right)+\left(I_b t_b\right)+\left(I_{EN}t_{EN}\right)} \qquad (8)$$

Once the melting rate, waveform, and other DBR measurements were made for each period, the BD was used to empirically determine α and β. The BD was demonstrated by Richardson (Ref. 15) as an efficient way to empirically determine the melting rate coefficients. A single line is yielded for CV processes (Fig. 2) that have a constant mode of transfer, like spray transfer, for a full range of operating conditions. The line produced on the BD for CV processes characterizes the effects of electrode extensions, wire feed speeds, and currents for that mode of transfer and electrode conditions. For the VP-GMAW process, this investigation showed that multiple BD lines were needed for each polarity depending on the waveform conditions. A separate burnoff diagram was created for each polarity, EN and EP, for the AC/MIG 200 power supply using the 1.14-mm steel electrode and 90%Ar-10%CO_2 shielding gas. For the EP period of different VP-GMAW waveforms, the lines were fitted between DBR measurements made in EPB and EPP periods. The coefficients measured in each waveform period were compared to prior research for EP heating, and used to establish the melting rate properties of EN, EPB, and EPP periods in VP-GMAW.

Results

The DBR method was used to measure the melting rate properties of each waveform period. The main focus was the EN period and waveform effects. Many measurements were taken to capture the relationship between I_{EN} and t_{EN} on the melting rate. Droplet burnoff rate measurements were also taken for the EP period, which used a constant pulse waveform. Here, separate DBR measurements were taken during the EPB and EPP periods until droplet detachment.

Table 2 — Summary of Melting Rate Coefficients for Steel Electrodes

Process	Electrode Diameter (mm)	Polarity	EN Time (ms)	α (mm-A^{-1}s^{-1})	β (10^{-4}, A^{-2}s^{-1})	Reference
CV Spray	0.8	EP		0.56	2.9	Lesnewich[13]
CV Spray	1.14	EP		0.25	0.7	Lesnewich
GMAW-P	0.8	EP		0.55	3.5–3.7	Richardson[15]
GMAW-P	1.0	EP		0.47	0.91	Richardson
GMAW-P	1.2	EP		0.27	0.59	Richardson
VP-GMAW	1.14	EN	0.0–5.9	0.80	5.9	
			6.0–8.0	0.80	6.0	
			9.0–11.9	0.72	5.4	
			12.0–14.8	0.78	4.2	
			14.9–17.9	0.85	2.9	
			18.0–23.3	0.82	2.9	
CV Spray	1.14	EP		0.28	0.9–1.0	
VP-GMAW	1.14	EP		–0.35–0.55	0.7–1.2	

EN Time Effects on Droplet Volume Growth Rate

Five I_{EN} and WFS combinations were studied to assess the effects of t_{EN}. The I_{EN} was constant for each WFS per Table 1 based on the pendant setting. The five different WFSs (42, 63, 84, 106, and 127 mm/s) were characterized at low %EN, which ranged from a minimum of 28 to 38%, to the highest %EN ranging from 67 to 81%. The AC/MIG 200 pendant settings for these times corresponded to 0 for low t_{EN} and 150 for the maximum t_{EN}. The lowest EN times were 3.1 and 8.3 ms at a 0 setting for WFSs of 127 and 42 mm/s, respectively. The highest t_{EN} were 18 and 23 ms at the 150 setting for the same WFS. The EN times were higher at the lower WFSs since the pulse frequency was lower. High-speed video was used to measure the droplet volume, V_d, as a function of t_{EN} at each WFS and 1_{EN} combination. The EN droplet volumes (Table 1) were measured by averaging 0.5 s of image data at 3700 frames/s. Typically, 10 droplets per condition were used for DBR measurements depending on the stability of the waveform and metal transfer. Pulse frequency at each WFS decreased as the %EN increased. The f range was small, only 35 to 42 Hz, at the low WFS of 40 mm/s. At 123 mm/s WFS, the f ranged from 38 to 91 Hz. The number of droplets available for measurement for each EN waveform condition, therefore, varied from 17 to 45 droplets since only 0.5 s of data were taken.

From the data in Table 1, there appeared to be a nonlinear relationship between Δx and V_d, as a function of t_{EN}. At long t_{EN}, the Δx saturated on average at about 10 ms of t_{EN} for wire feed speeds greater than 63 mm/s. The V_d continued to grow but at a slower rate once saturated. The change in droplet growth rate, V_D, was related to t_{EN} by evaluating the droplet volume growth rate. The V_D was typically higher at short t_{EN} for constant I_{EN}. This was especially true for the higher WFS tests. The melting rate for the EN period was heavily dependent on Δx. Here, Δx was a larger part of the MR at short t_{EN}. Since there was a nonlinear relationship between I_{EN} and MR as a function of t_{EN}, additional image analysis was performed on three droplets from the low and high t_{EN} from each WFS test group. The droplets that were selected had uniform arc initiation and were considered ideal. The V_d was graphed during the whole EN period by continuously accounting for the WFS and Δx in each high-speed video frame as a function of time. The graphs shown in Fig. 4A and B were plotted to evaluate how V_d grows with time; the magnitude of growth rate, V_D, and compare the effects of t_{EN} at constant I_{EN}. The results from three drops were averaged and plotted in Fig. 4A (low t_{EN}) and 4B (high t_{EN}) for each WFS and I_{EN} combination. The line fitted in each graph was the average incremental droplet volume over time. The slope of the line equaled the droplet volume growth rate, V_D. At WFS of 42 mm/s, V_D was 40.4 and 26 mm^3/s for low and high t_{EN}, respectively, as shown in Fig. 4A. I_{EN} for this WFS was 40 A. The V_D increased to 325.4 and 188.5 mm^3/s at low and high t_{EN}, respectively, for 123 mm/s WFS and I_{EN} = 133 A, as shown in Fig. 4B. In all these tests, the low t_{EN} produced a higher V_D compared to long t_{EN}, at the same current. These data were similar to the Table 1 measurements, which averaged a 0.5 s of high-speed video data, especially for the higher WFS test groups. The line slopes measured from the Fig. 4 graphs, which equaled the V_D rate, had an average coefficient of multiple determination (R^2) of 0.957, which indicated a good data fit.

DBR Measurements for the EN Period

The DBR method was used to measure the MRs for the test matrix in Table 1, which had five different WFSs (42, 63, 84, 106, and 127 mm/s) at six different %EN levels. The corresponding pendant settings were 0, 30, 60, 90, 120, and 150. Since the melting rates were sensitive to t_{EN}, the results were separated into groups for plotting. The t_{EN} groups were 3 to 5.9, 6.0 to 8.9, 9.0 to 11.9, 12.0 to 14.8, 14.9 to 17.9, and 18.0 to 23.2 ms. These were basically 3-ms groupings except for the last. The average MR_{EN}, L_{EN}, and I_{EN}, and time at each waveform condition were used to calculate the BR and F_L. These results were plotted to construct the BD (Fig. 5), which was used to solve for the melting rate coefficients. The y-axis intercept was equal to the arc melting coefficient, α_-, and the slope of each line was equal to the resistive heating coefficient, β_-. The overall shape of this graph showed a burnoff rate range that increased as F_L increased instead of a single line. This was the opposite of a CV BD where a single line is produced describing the melting rate behavior of a GMAW consumable set. The lines in Fig. 5 were fitted to the data and were based on the 3-ms t_{EN} increments at each EN current. This approach was used based on the dependency on V_D to t_{EN} that was established during data analysis. The highest burnoff rates as a function of heating factor, F_L, were achieved at the lowest t_{EN}. Likewise, long t_{EN} showed a decrease in BR. Comparing the equations that were solved for each line shows β_- varied from 2.9 to 6.0 x 10^{-4}, A^{-2}s^{-1}.

These units were large for β. This was not expected since polarity should not affect the resistivity of the electrode. A theory was developed to explain why β_- was dependent on t_{EN} for the EN period. The increase in melting rate at short t_{EN} was believed to be due to a concentrated melting effect. Careful observation of the high-speed video data showed that the EN arc rapidly climbed the electrode tip; the extent depended on the current level. The electrode tip that was covered by the EN arc rapidly melted and promoted higher V_D in the initial part of the EN period. The Δx saturated as the t_{EN} increased at constant I_{EN} and WFS. The large droplet that was formed decreased the melting effect of the cathode arc at long t_{EN} since the arc concentrated on it. This theory was supported by Norrish (Ref. 34) who observed

Table 3 — BDR Measurements for EP Waveforms

Weld No.	WFS_{DAQ} (mm/s)	Δx (mm)	t_p or t_b (s)	$\Delta x/t_p$ or $\Delta x/t_b$ (mm/s)	MR (mm/s)	V_d (mm^3)	V_D (mm^3/s)	I_p or I_b (A)	BR (mm/(s A))	F_L (mm A)	f (Hz)	EPP or EPB Period (%)	V_{pp}- (prepulse) (mm^3)
B-0-42	39.09	–0.273	0.0119	–22.890	16.20	0.198	16.62	25.19	0.430	320.88	41.75	49.81	0.39
B-90-42	38.94	–0.057	0.0015	–37.708	1.23	0.002	1.27	24.81	0.028	318.72	39.51	5.97	0.39
B-0-127	123.28	–0.115	0.0009	–125.521	–2.24	–0.002	–2.30	46.46	–0.051	595.50	91.09	8.36	0.39
B-90-127	123.31	–0.221	0.0016	–141.286	–17.97	–0.029	–18.44	46.12	–0.315	588.69	49.68	7.78	0.39
P-0-42	39.09	0.500	0.0016	303.535	342.63	0.579	351.56	362.08	0.980	4752.26	41.75	6.87	0.78
P-90-42	38.94	0.424	0.0030	142.661	181.60	0.553	186.34	365.32	0.497	4780.87	39.51	11.73	1.05
P-150-42	38.84	0.184	0.0023	81.325	120.17	0.280	123.30	365.39	0.407	4738.09	34.72	7.87	1.38
P-0-127	123.28	–0.130	0.0053	–24.338	98.95	0.541	101.53	373.14	0.267	4779.97	91.09	48.56	1.11
P-90-127	123.31	–0.556	0.0044	–125.595	–2.28	–0.010	–2.34	381.48	–0.008	4805.50	49.68	21.99	2.86
P-150-127	123.97	–0.617	0.0047	–132.507	–8.56	–0.041	–8.79	382.26	–0.022	4803.67	38.20	17.79	3.78

Notes:
1) Weld No. code defines EP period — pendant setting, wire feed speed (mm/s).
2) For EP period: B indicates background period and P indicates peak period from that test.
3) The pendant setting of 150 had no background period to measure.
4) Prepulse droplet volume, V_{pp}, was measured from high-speed video DBR plus postpulse remainder of 0.39 mm^3.

that a constant voltage EN arc can oscillate between a multispot and single-spot cathode as the droplets form and detach, respectively.

The burnoff rate in Fig. 5 was heavily dependent on the Δx based on the measurements in Table 1. The electrode extension burnoff was up to 50% of the total melting rate at low t_{EN}, especially at the higher I_{EN} and WFSs. Since higher BR results in large changes in line slope, the effect was measured by the β_- coefficient. Since the electrode extension became shorter when including the burnoff effect, F_L decreased. This would increase the slope of the lines too. Therefore, Δx acts to increase the slope of the burnoff diagram based on its effect on both graph parameters, BR and F_L.

Melting Rate Measurements for the EP Period

Burnoff diagrams for a given electrode type and diameter are linear for EP constant voltage processes for a large range of currents, arc length, and CTWDs. This is true as long as the metal transfer mode is constant, especially for the spray transfer mode since it develops a very stable electrode tip that is covered by the arc and employs free-flight metal transfer. A separate set of spray GMAW tests were performed to verify the relationships that were established by Lesnewich and Richardson (Refs. 13, 15). This set of experiments simply tested the effects of several WFSs and arc lengths at 16 and 19 mm CTWD. The BD from these tests was plotted and found to yield a linear relationship for the entire group of tests — Fig. 2. Here, the α was 0.28 $mm\text{-}A^{-1}s^{-1}$ and the β was 0.9 to 1.0 x 10^{-4}, $A^{-2}s^{-1}$. The α and β coefficients were in good agreement with the measurements provided by Lesnewich (Ref. 13) for spray as shown in Table 2. This simple set of tests reinforced the use of the BD for solving melting rate relationships.

DBR Measurements for EP Pulse

Measurements made on the EP period of the VP-GMAW waveforms were found to be difficult. The major challenge was accommodating the wide range in light intensity during the current pulse, the EPP period, while following the position of the electrode extension-droplet neck. The image analysis software helped filter the light intensity of recorded images, but the contrast was too great during the full peak current to locate the solid-liquid interface if the arc expanded over the droplet. Even though improvement can still be made to the high-speed video equipment, enough good images were obtained at several waveforms to study the EPP period in VP-GMAW. Visual observation of the melting process yielded some important results. The EPP pulse arc rapidly climbed the electrode tip above the droplet when the droplet was small. As the arc covered the electrode, rapid melting occurred. An entire column of electrode above the droplet was observed to melt and mix with the droplet on pulses where the arc grew on the electrode extension. The droplet started to neck in most cases before finishing the EPP period. Likewise, different arc behavior was observed when the droplet size was large. Here, the EPP pulse arc rooted and could not expand over the bottom of large droplets. Once the neck started for droplet detachment, the peak current arc followed the detaching drop toward the weld pool. This resulted in some solidification at the electrode tip as the neck broke and before arc reattachment to the electrode tip. Therefore, the melting efficiency of the EP period was largely related to the prepulse droplet size. This behavior influenced MR_{EP} and Δx where the values were negative for large prepulse droplets (Table 3).

Detailed DBR measurements for EP periods were performed on 10 different conditions (Table 3). The WFS conditions represented the range of background and peak conditions that were observed with the VP-GMAW waveforms. The EN pendant settings of 0, 90, and 150 resulted in %EN range of 34 to 81% for 42 mm/s, and 28 to 69% for 127 mm/s tests. An EPB period was only measured on EN pendant settings of 0 and 90. At both WFSs, the 150 pendant setting resulted in a waveform that had no EPB time and alternated between EPP and EN pulses. The DBR measurements were calculated for both the EPB and EPP periods. The background time t_b was equal to the time for that period. For the EPP period, the time t_p was from the period beginning until drop detachment of the first drop per Fig. 1. This was factored to accommodate the large change in electrode melting rate that occurred during the current pulse and at drop detachment. The BD was plotted from the data in Table 3 and used to solve the arc and resistive heating coefficients — Fig. 6. Lines were fitted between DBR measurements that had both EPB and EPP periods for that waveform. The points on the left side of this figure were from EPB measurements and the right side were from EPP measurements. From these lines it was obvious that EP pulse melting rate coefficients were not constant. The change in α_+ coefficients was related to the prepulse droplet volume — Fig. 7. The droplet volume immediately after detachment was measured and ap-

proximated to be 0.39 mm^3 for most waveforms. The droplet was approximately equal to a half hemisphere based on the wire diameter immediately after detachment and starting into a new period. This assumption was made to account for the arc behavior observed in the high-speed video images.

Discussion

As shown in Fig. 2, the BD for EP constant voltage produced a linear burnoff relationship for a range of electrode extensions, WFSs, and current conditions. The second-order melting rate relationship described by Equation 1, which was developed by Lesnewich (Ref. 13) and verified by Richardson (Ref. 15), was verified here too. Based on these data, the BD can be used to determine melting rate coefficients for GMAW processes that have a stable mode of transfer, like spray transfer.

The DBR method evaluated the direct relationship between the arc current waveform and electrode droplet melting rate. Synchronized high-speed video was used to measure droplet melting, growth, and detachment in each waveform period, EN, EPB, and EPP. Best fit lines were used to trend the data on the BD for the EN period as a function of t_{EN} range (Fig. 5), and for the EP pulse period as a function of prepulse droplet volume — Figs. 6 and 7. This was performed to explain the variation in electrode melting rate with VP-GMAW waveforms.

A summary of arc and resistive heating coefficients was prepared for comparison (Table 2). For GMAW-P, Richardson determined the resistive heating coefficient, β_+, equaled 0.59×10^{-4}, $A^{-2}s^{-1}$ for 1.2-mm steel electrodes. For CV GMAW, Lesnewich determined β_+ to equal approximately 0.7×10^{-4}, $A^{-2}s^{-1}$ for steel at this wire diameter. The resistive heating coefficient is dependent on electrode cross section and resistivity, so different values would be expected if different sizes and types of electrodes were tested. However, it was not expected that β values would be different for EN and EP periods with constant electrode conditions. At the very longest t_{EN} groups shown in Table 2, the β_- values for the EN period decreased enough that they were near the values measured by Richardson for GMAW-P for smaller electrodes. Overall, the β_- coefficients were three to six times greater than the values reported by Lesnewich for CV GMAW. Since β_- varied in these tests, the results from the BD based on the DBR method were physically not linked to the arc melting and resistive heating coefficients as defined per Equation 1 by Lesnewich. Here, the BD provided a simple tool for solving for coefficients used in second-order polynomials for each period. It was not believed that resistive heating changed with polarity. The slope of the lines in Fig. 5, which equal β_-, increased since BR increased and F_L decreased when t_{EN} decreased at constant I_{EN}. This behavior was related to the concentrated melting theory that is based on the transient behavior between the growing droplet and the arc. The arc heat used for melting changed based on the conditions between the forming droplet and the arc, but the BD measures these changes by slope changes. The β_- data fit was good except at the lower WFSs and I_{EN}s as shown in Fig. 5. Linear lines were used to simply solve for the melting rate coefficients. A higher-order polynomial may have provided better fit for the lower I_{EN} data. Ignoring the low I_{EN} data, the intercept of the lines for the EN burnoff diagram varied little. The variation in data line fit was attributed to grouping t_{EN} into 3-ms groups. This data grouping was based on fitting the measured t_{EN} from incremental %EN pendant test settings that were used at each WFS.

The α_- (intercepts in Fig. 5) were significant and were almost constant for all the t_{EN} groups. Average α_- was approximately 0.8 $mm\text{-}A^{-1}s^{-1}$ and ranged from 0.72 to 0.85 $mm\text{-}A^{-1}s^{-1}$ (Table 2). For comparison, α_+ for GMAW-P and CV GMAW was 0.27 and 0.25 $mm\text{-}A^{-1}s^{-1}$, according to Richardson and Lesnewich, respectively. The α_- data were more than three times greater than α_+ measurements made by the prior researchers, which demonstrates the melting potency of an EN arc.

The β_+ determined from Fig. 6 varied from 0.7 to 1.2×10^{-4}, $A^{-2}s^{-1}$ over the test conditions. As shown in Table 2, Lesnewich determined β_+ to equal approximately 0.7×10^{-4}, $A^{-2}s^{-1}$ at this wire diameter for steel CV GMAW. Independent CV GMAW spray measurements performed in this investigation found β_+ equaled to 0.9 to 1.0 $A^{-2}s^{-1}$. Therefore, the β_+ determinations for the EP pulse period were within the range and agreed with CV spray measurements. β_+ did increase slightly with decreasing prepulse droplet volume.

The α_+ coefficients were both positive and negative and varied from –0.35 to 0.35 $mm\text{-}A^{-1}s^{-1}$ for the different VP-GMAW conditions. As shown in Table 2, the α_+ coefficients for GMAW-P and CV GMAW spray were 0.27 and 0.25 $mm\text{-}A^{-1}s^{-1}$ for 1.2- to 1.14-mm electrodes per Richardson and Lesnewich, respectively. The large α_+ differences determined for the VP-GMAW process were attributed to the large range of prepulse droplet volume produced with different EN period waveforms.

The droplet volumes plotted in Fig. 7 were calculated from the high-speed video data just before entering the peak pulse period (Table 3). These measurements were scaled to include the droplet remainder immediately after detachment from the previous pulse. As mentioned earlier, the arc rapidly climbed the electrode tip as the current was pulsed when the droplet was small. This provided concentrated melting of the electrode extension where the arc covered it. However, large droplets inhibited further melting of the electrode tip, and this effect was shown by the negative α_+ data. Large droplets significantly reduced arc melting because the arc was rooted on the droplet bottom. A negative coefficient indicated that the electrode extension was increasing in length and the arc length was decreasing.

Concentrated Melting Theory

A theory was developed to describe the dependency of electrode melting rate in VP-GMAW on 1) EN time at constant EN current, and 2) the prepulse droplet volume for EP pulsing. The theory was named the "concentrated melting theory" and is defined as follows:

"The melting potency of GMAW current waveforms is strongly dependent on arc concentration at the electrode tip above the droplet interface, and the droplet size and growth process. Virgin electrode metal is consumed rapidly when the arc is permitted to climb over and concentrate on the electrode extension. Droplet growth is rapid in current transients when the arc climbs the electrode tip causing extension burnoff. During a waveform constant current period, the electrode melting rate decreases once the burnoff is complete and the droplet size inhibits further arc concentration and climb on the electrode. Once the arc is rooted on the droplet bottom, the electrode melting rate will continue to decrease as the droplet grows until drop detachment."

The concentrated melting theory applies to open-arc GMAW processes that employ current waveform that pulse the current and/or polarity to regulate metal transfer. Droplet transfer in VP-GMAW occurred during the EP pulse. Observations made during high-speed video analysis found that the EN arc climbed over the electrode tip (Fig. 3), which had a small droplet remainder, as soon as the current switched polarity and the EN arc was ignited. The arc cathode was distributed over a large electrode tip area. This was quite different from the CV processes like spray transfer where the arc is stable and continuously covers a portion of the electrode tip. This EN arc behavior was also observed by Norrish (Ref. 34). In steady-state EN GMAW, Norrish observed that the arc formed a multispot cathode that

climbed the electrode after drop detachment. Once a droplet formed, the arc switched to a single spot cathode mode and rooted on the droplet bottom. The observations by Norrish reinforce the concentrated melting theory for EN waveforms.

Higher EN currents promoted larger arc plasmas that covered more of the solid electrode extension tip. The electrode extension area that was enveloped by the EN arc melted early in the EN period. Once a large droplet formed, the electrode melting rate decreased because the arc concentrated the heat on the droplet. Therefore, high current waveforms that used low EN time had much larger droplet volume growth rates, V_D, compared to long EN times as shown in Fig. 4. Droplet growth rate was dependent on the concentrated melting based on the size of the arc plasma and time. Once the electrode extension burnoff saturated, the melting rate decreased since the arc was concentrated on the droplet instead of solid electrode. Analysis of the high-speed image data showed that the electrode extension meltback was the greatest at the beginning of the EN period (Table 1). At EN times up to 20 ms, the change in electrode extension, Δx, saturated at 9 to 11 ms into the period for EN currents that were 60 A or higher.

The concentrated melting theory also applied to EP pulse waveforms. The prepulse droplet volume had a significant effect on the α_+ coefficient. High-speed video images were taken to show how the prepulse droplet affected the electrode extension burnoff. When the prepulse droplet volume was small, the arc was observed to rapidly climb as the current increased over the electrode tip behind the droplet as shown in Fig. 8. A column of electrode would collapse and mix with the droplet. The arc eventually became rooted on the droplet that grew from electrode melting and extension burnoff. Further electrode melting was limited when the detachment process started with the formation of a neck. The arc followed the droplet through the detachment process. A decrease in melting rate was observed during the necking process where the electrode tip was observed to solidify after the droplet bridge ruptured, and at the same time the arc length shortened. The arc would then jump to the electrode tip after drop detachment to maintain the circuit where a new droplet was initiated. Large prepulse droplets completely blocked the EP pulse arc from climbing on the electrode extension — Fig. 9. Here, the electrode melting rate was significantly reduced during the EPP pulse providing no additional electrode extension burnoff. As the neck formed, the arc followed the detaching drop. The tip of the electrode partially solidified during the rupture of the neck since the arc was removed. These visual observations together with the DBR data show that the melting rate of VP-GMAW waveforms was strongly dependent on the transient behavior between the arc in each period and the droplet formation process. The prediction of VP-GMAW melting rate (Ref. 12) required detailed understanding of these mechanisms.

A source of error was fume generation from droplet heating once the arc rooted on it. Since droplet volume calculations per Equation 3 were proportional to the sum of the WFS_{DAQ} and $\Delta x/t$, there was no term added to subtract fume losses. This is an area for future work and further development of the DBR method. The true droplet volume also could not be measured from the high-speed video since the droplet profile oscillates during welding and does not provide a perfect sphere for video analysis. With respect to fume, Ushio showed that VP-GMAW produced significantly less fume compared to GMAW-P and CV GMAW on aluminum alloys (Refs. 35, 36). Based on the data developed here for steel, it is believed that fume losses are probably minimized with VP-GMAW for steel, too, since the melting rates are so much higher than CV GMAW and GMAW-P. On future welding applications, optimized waveforms that minimize droplet heating by controlling the duration of the waveform periods relative to the droplet growth and detachment process will provide a lower fume process.

Conclusions

1. Melting rate was very dependent on current waveform, polarity, and droplet size, and metal transfer events if they occurred, during each waveform period. The transient conditions of current waveform and metal transfer produced rapid changes in arc behavior, which strongly influenced the melting rate for each period of various VP-GMAW waveforms.

2. The concentrated melting theory was developed to explain the significant increase in electrode extension burnoff and droplet growth rate that occurred at short EN time as a function of current, and during EP peak pulse when the prepulse droplet volume was small. The highest electrode extension burnoff and droplet growth rate occurred when the arc was permitted to climb over the solid electrode tip producing rapid concentrated melting. Likewise, large molten droplets were found to promote a negative electrode extension burnoff and a decreased droplet growth rate. The arc rooted on large droplets providing additional heating but limited additional electrode melting.

3. The DBR method was found to yield good experimental measurements for α and β coefficients used in melting rate equations for complex waveforms like those used in VP-GMAW. The coefficients were not as physically linked to α and β, like the prior research, but provided characterization of second-order behavior for electrode melting rate in each period of the waveform.

4. EN time affected the melting rate as a function of EN current. The melting rate contribution from electrode extension burnoff increased as the EN time decreased in a range from 23 to 3 ms. This was measured by the change in the β_- coefficient. This change was related to the slope of the burnoff diagram, which increased when burnoff rate increased as a result of electrode extension burnoff.

5. The melting rate of the EP periods, both background and peak, were related to the prepulse droplet volume. Large prepulse droplets, which formed in the EN period, decreased the EP melting rate since the arc concentrated more on the droplet than above it on the unmelted electrode extension. The arc was observed to follow the droplet during detachment and some solidification of the molten tip occurred before the arc reattached to the tip at drop transfer. This reduced the electrode melting rate of EPP periods.

6. For EP pulse waveforms, the prepulse droplet volume effect on melting rate was measured by a change in the α_+ coefficient, which was negative for some DBR measurements that had large prepulse droplet volumes. The negative influence was not a result of reduced heating, but a result of preferential heating of the droplet instead of melting the electrode tip. The electrode extension increased under these conditions resulting in a shorter arc length.

Acknowledgments

Edison Welding Institute (EWI) sponsored this collaborative dissertation project at Cranfield University's Centre for Welding Research. OTC Daihen Robots is acknowledged for provided the welding equipment.

References

1. Ogasawara, T., Maruyama, T., Saito, T., Sato, M., and Hida, Y. 1987. A power source for gas shielded arc welding with new current waveforms. *Welding Journal* 66(3): 57–63.

2. Maruyama, T., Okada, M., Hida, Y., Honma, M., and Minato, T. 1995. Current waveform control in gas shielded arc welding for robotic systems. Kobelco Technology Review, No. 18, April, pp. 10–14.

3. Nacey, T. 1995. The effect of dynamic variables on GMAW arc characteristics — Controlling the power supply response. *The Fabri-*

cator 25(2): 18–20.

4. Nacey, T., and Pagano, K. 1995. Advancements in DC and AC low current pulse GMAW. *Proceedings from ICAWT 11th Annual Conference,* Columbus, Ohio, Paper No. 2-3(C).

5. Maruo, H., and Hirata, Y. 1988. MIG welding with rectangular wave AC. Technology Reports of the Osaka University. Vol. 38(1935): 237–245.

6. Maruyama, T., et al. 1988. Polarity ratio control GMA welding power source, data for the JWS 118th Welding Method Research Committee.

7. Tanimoto, J., Minooka, M., and Nishida, Y. 1988. Development of the AC pulsed MAG welding process. IIW Asian Pacific Regional Welding Congress, 36th Annual AWI Conference.

8. Okada, M. 1989. Sensarc PC350 EP/EN ratio-controllable GMA welding power source. Masashi OKADA, Welding Equipment Robot Department, Welding Division, Kobelco Technology Review, No. 6.

9. Okada, M. 1992. Sensarc AL350 penetration-controllable MIG welding power source for aluminum alloy. Kobe Steel, Factory Automation and Robotics Group, New Business Division, Kobelco Technology Review, No. 6.

10. Harada, S., Ueyama, T., Mita, T., Innami, T., and Ushio, M. 1999. The state-of-the-art of AC-GMAW process in Japan. *IIW Doc. XIII-1589-99*, pp. 1–10.

11. Ueyama, T., Tong, H., Harada, S., and Ushio, M. 2000. Improve sheet metal welding quality and productivity with AC pulsed MIG welding system. *IIW Doc. XII-1629-00*, pp. 86–102.

12. Harwig, D. D. 2003. Arc behavior and metal transfer in the VP-GMAW process. PhD dissertation, Cranfield University.

13. Lesnewich, A. 1958. Control of melting rate and metal transfer in gas-shielded metal arc welding — Part I — Control of electrode melting rate. *Welding Journal* 37(8): 343-s to 353-s.

14. Allum, C. J. 1983. MIG welding- time for a reassessment. *Metal Construction*, pp. 347–353.

15. Richardson, I. M., Bucknall, P. W., and Stares, I. 1994. The influence of power source dynamics on wire melting rate in pulsed GMA welding. *Welding Journal* 73(2): 32-s to 37-s.

16. Amin, M. 1981. Synergic pulse MIG welding. *Metal Construction*, June, pp. 349–353.

17. Amin, M. 1983. Pulse current parameters for arc stability and controlled metal transfer in arc welding. *Metal Construction*, May, pp. 272–278.

18. Nixon, J. H., and Norrish, J. Determination of pulsed MIG process parameters. *Synergic MIG Supplement*, pp. 4–7, Pulse Parameters for XMT 300 CC/CV.

19. Kim, Y. S., and Eagar, T. W. 1993. Metal transfer in pulsed current gas metal arc welding. *Welding Journal* 72(7): 279-s to 287-s.

20. Joseph, A. 2001. Assessing the effects of GMAW pulse parameters on arc power and weld heat input. Masters thesis, The Ohio State University, Columbus, Ohio.

21. Lucas, W., and Needham, J. C. 1975. Why not AC MIG-welding? *The Welding Institute Research Bulletin*, March, pp. 63–67.

22. Lucas, W. 1978. Solid wire AC MIG welding. *Welding Research International* 8(2): 102–127.

23. Dymenko, V. V., and Zaruba, I. I. 1979. Stabilizing the arc discharge during welding with AC. *Automatic Welding* 31(3): 25–29.

24. Nakanishi, M., Katsumoto, N., Komizo, Y., Hasunuma, S., and Seta, I. 1983. Development of AC MIG arc welding. *The Sumitomo Search*, No. 28, October, pp. 73–86.

25. Tsushima, S., and Fujita, H. 1992. Pulse generator for high-current AC-MIG welding process — Development of AC-MIG welding process (Report 2).

26. Tsushima, S., Ohkita, S., and Horii, Y. 1992. Effects of oxygen on the toughness of Ti B containing AC MIG weld metal — Development of AC MIG welding process (Report 3). pp. 56–63.

27. Tsushima, S., and Kitamura, M. 1994. Tandem electrode AC-MIG welding — Development of AC-MIG welding process (Report 4). *Welding International* 8(8): 599–605.

28. Tsushima, S., Horii, Y., and Yurioka, N. 1994. Application of AC-MIG narrow-gap welding to butt joints in 980 MPa high-strength steels (5th Report) —Development of AC-MIG welding. *Welding International* 8(7): 525–531.

29. Talkington, J. E. 1998. Variable polarity gas metal arc welding. The Ohio State University, Columbus, Ohio, thesis.

30. Ushio, M., Nakata, K., and Tanaka, M. 2000. AC pulsed GMA welding of Al-Mg alloy — Fume and welding arc phenomena. Productivity Beyond 2000, IIW Asian Pacific Welding Congress, The WTIA 43rd National Welding Congress, pp. 859–873.

31. Ushio, M., Nakata, K., Tanaka, Tong, H., and Mita, T. 1994. Fume generation in Al-Mg alloy welding with AC-pulsed GMAW welding method. *Trans. of JWRI* 23(1).

32. Harwig, D. D., Joseph, A., and Dierksheide, J. E. 2002. Capability of variable polarity GMAW for automotive applications. AWS Sheet Metal Welding Conference X, Detroit, Mich., May 15–17.

33. Harwig, D. D., Joseph, A., Anderson, C., and Moore, J. 2000. Characteristics of variable polarity (AC) GMAW power supplies. *Proceedings from ICAWT 2000*, AWS, Orlando, Fla., Dec. 6–8.

34. Norrish, J. 1974. High deposition MIG welding with electrode negative polarity. *Proceedings from 3rd Intl. Conf. on Advances in Welding Processes*, The Welding Institute, May 7–9, pp. 121–128.

35. Ushio, M., Nakata, K., and Tanaka, M. 2000. AC pulsed GMA welding of Al-Mg alloy — Fume and welding arc phenomena. Productivity Beyond 2000, IIW Asian Pacific Welding Congress, The WTIA 43rd National Welding Congress, pp. 859–873.

36. Ushio, M., Nakata, K., Tanaka, Tong, H., and Mita, T. 1994. Fume generation in Al-Mg alloy welding with AC-pulsed GMAW welding method. *Trans. of JWRI* 23(1).

CAN WE TALK?

The *Welding Journal* staff encourages an exchange of ideas with you, our readers. If you'd like to ask a question, share an idea or voice an opinion, you can call, write, e-mail or fax. Staff e-mail addresses are listed below, along with a guide to help you interact with the right person.

Publisher/Editor
Andrew Cullison
cullison@aws.org, Extension 249
Article Submissions

Senior Editor
Mary Ruth Johnsen
mjohnsen@aws.org, Extension 238
Feature Articles

Associate Editor
Howard Woodward
woodward@aws.org, Extension 244
Society News
Personnel

Assistant Editor
Kristin Campbell
kcampbell@aws.org, Extension 257
New Products
News of the Industry

Managing Editor
Zaida Chavez
zaida@aws.org, Extension 265
Design and Production

Advertising Sales Director
Rob Saltzstein
salty@aws.org, Extension 243
Advertising Sales

Advertising Sales & Promotion Coordinator
Lea Garrigan Badwy
garrigan@aws.org, Extension 220
Production and Promotion

Advertising Production Manager
Frank Wilson
fwilson@aws.org, Extension 465
Advertising Production

Peer Review Coordinator
Doreen Kubish
doreen@aws.org, Extension 275
Peer Review of Research Papers

Welding Journal Dept.
550 N.W. LeJeune Rd.
Miami, FL 33126
(800) 443-9353
FAX (305) 443-7404